A computational study on compressor inlet restriction to suppress surge instabilities in turbochargers

Rick Dehner[a], Ahmet Selamet[b], Emel Selamet[c] and Keith Miazgowicz[d]

(Received: 19 October 2020; Revised: 12 February 2021; Accepted: 5 March 2021)

Operation of centrifugal compression systems below their stability limit causes surge to occur, resulting in large amplitude pressure fluctuations near the natural frequency of the system. Deep surge in the compression system of turbocharged internal combustion engines degrades performance and drastically increases noise. The current computational work demonstrates elimination of surge instabilities by incorporating sufficient restriction at the inlet of a turbocharger compressor. Both one-dimensional (1D) gas dynamics and three-dimensional (3D) computational fluid dynamics (CFD) models were developed to study the impact of a flow restriction on the amplitude of pressure and mass flow rate fluctuations and, therefore, system stability. The analyses were performed at a fixed operating point with a (time-averaged) mass flow rate below the deep surge boundary. As the inlet restriction was partially closed with the 1D model, the compression system remained in deep surge over a majority of the area ratio (of restriction to adjacent duct) range, and the amplitude of mass flow rate fluctuations gradually reduced with decreasing area of restriction. With sufficient inlet restriction, pressure and flow rate fluctuations were eliminated and the system was stabilized. In order to gain further insight into the importance of multi-dimensional physics, a simulation with the 3D model was carried out. Qualitatively, the 1D and 3D modeling results at equal pressure drop across the restriction were found to be similar. These unsteady predictions highlight the role of mass balance in the intermediate volume (between the restriction and compressor) toward reducing the amplitude of mass flow rate fluctuations. ***© 2021 Institute of Noise Control Engineering.***

Primary subject classification: 11.6.2; Secondary subject classification: 13.2.1

1 INTRODUCTION

Surge instabilities result in pressure and flow rate fluctuations throughout the compression system and limit the low-flow operating range of centrifugal compressors. In 1955, Emmons et al.[1] provided a fundamental description of surge physics by capturing velocity fluctuations throughout the entire compression system ducting. Their work also laid the groundwork for future developments by identifying that fluctuations due to surge instabilities occur near the natural frequency of the compression system, which corresponds to the Helmholtz resonance frequency for the typical duct-plenum (volume) configuration (excluding inlet restriction) shown in Fig. 1. In addition, surge instabilities can be further characterized as "mild" or "deep." During mild surge, the mass flow rate throughout the compression system oscillates, but the cross-sectional average remains in the forward direction at all times. However, during deep surge, the cross-sectional average flow rate reverses direction over a portion of the cycle. The amplitude of pressure fluctuations increases dramatically when a compression system transitions from mild to deep surge, which results in loss of performance, increased levels of noise, and potential mechanical failure of the compressor.

In the 1970s, Yano et al.[2] and Greitzer[3] formulated lumped parameter (also, zero-dimensional or 0D) compression system models that identified the impact of compression system geometry on unsteady surge cycles.

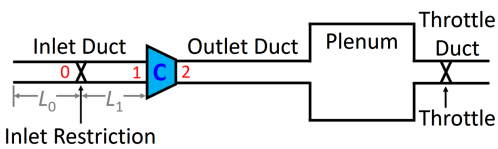

Fig. 1—Simplified compression system.

[a] Department of Mechanical and Aerospace Engineering, The Ohio State University, Columbus, OH; email: dehner.10@osu.edu
[b] Department of Mechanical and Aerospace Engineering, The Ohio State University, Columbus, OH; email: selamet.1@osu.edu
[c] Department of Mechanical and Aerospace Engineering, The Ohio State University, Columbus, OH; email: selamet.2@osu.edu
[d] Ford Motor Company, Global Engine Engineering, Dearborn, MI.

These lumped models were formulated for the simplified duct-plenum (excluding inlet restriction) configuration in Fig. 1. Greitzer[3] demonstrated that surge instabilities are possible when the compressor operates on the positive sloped $dPR_{c,ts}/d\dot{m}$ portion of the constant rotational speed total-to-static pressure ratio $PR_{c,ts}$ versus mass flow rate $\dot{m}$ characteristics.

It was recently demonstrated experimentally[4] that surge instabilities can be suppressed by coupling a slight flow restriction with the compressor, as depicted in Fig. 1. Experimental results with the restricted compressor inlet system demonstrated a shift of the (deep) surge line to mass flow rates of approximately one-third of those for the corresponding unrestricted system. The amount of restriction required to eliminate surge instabilities varied based on the local slope of the compressor alone characteristic.

A theoretical analysis was also presented[4], which treated the restriction as a simple concentric orifice. This analytical work demonstrated how coupling between the compressor and inlet restriction occurs in a manner similar to stages in a multi-stage turbomachine. The effective pressure ratio,

$$PR_{\text{eff,ts}} = PR_{\text{r,tt}} PR_{\text{c,ts}}, \tag{1}$$

of this system is the product of the pressure ratios for the restriction ($PR_{r,tt} = p_{t.1} / p_{t,0}$) and compressor ($PR_{c,ts} = p_2 / p_{t,1}$). Flow restrictions inherently stabilize the system since the pressure ratio decreases (pressure drop increases) as the mass flow rate is elevated. Therefore, the restriction alone pressure ratio versus mass flow rate characteristics exhibit a slope that is always negative $\left(dPR_{r,tt}/d\dot{m}\right) < 0$, and the slope becomes further negative with increased restriction (pressure drop). The combined (restriction plus compressor) system was assumed to operate without surge when $\left(dPR_{\text{eff,ts}}/d\dot{m}\right) \leq 0$,where $\dot{m}$ is the mass flow rate through the restriction and compressor. A parametric study of the restriction flow area was utilized to illustrate further extension of the compressor low-flow operating range with additional restriction. The analytical model provided a useful insight into the stabilizing aspect of coupling between the restriction and compressor, and it correctly predicted the trends of restricted compressor inlet stability with reasonable accuracy. However, this simple model did not allow for estimation of the amplitude of surge instabilities (in regions where they were predicted to occur). In addition, the theoretical analysis assumed that the axial distance (L_1 in Fig. 1) was short between the restriction and compressor inlet, and as formulated, this approach[4] is unable to capture the impact of L_1 (or other geometry) on system stability.

Surge modeling capabilities were previously developed for the *unrestricted* compression system with one-dimensional (1D) gas dynamics[5–10] and three-dimensional (3D) computational fluid dynamics (CFD)[10–12] models of an experimental setup. The 1D and 3D models were validated using experimental data while operating in the stable range, and the mild and deep surge instability regions. The modeling results agreed favorably with experimental data, in terms of capturing the amplitude and frequency of pressure and flow rate fluctuations, as well as the boundaries between stable, mild, and deep surge operation.

The present work builds upon these 1D and 3D surge modeling capabilities by incorporating the compressor inlet restriction. Due to the inherent advantages and disadvantages of each modeling approach, the objectives are different. The fast computational time of 1D models allows for a detailed parametric analysis to explore the impact of restriction at a fixed operating point that is within the deep surge region of the unrestricted (typical) compression system. The computational time of the 3D CFD model is extensive, but it captures multi-dimensional physics that are not possible with 1D tools. Therefore, 1D predictions are utilized to understand how the system behavior changes with variable levels of compressor inlet restriction and, ultimately, determine the threshold of restriction required to eliminate surge instabilities. The 3D CFD model is then utilized to explore active stabilization at a restriction pressure drop that rapidly eliminated surge with the 1D model. Therefore, the inlet restriction of the 3D CFD prediction is equivalent (equal pressure drop) to that from one of the selected cases in the 1D study. As a result, a one-to-one comparison can be made to evaluate the implications of 1D assumptions and to analyze multi-dimensional aspects of the flow field. The primary objectives of these computational studies are (1) to assess the feasibility of using 1D and/or 3D tools to model restricted compressor inlet systems and (2) to further the understanding of the physics that results in stabilization of the compression system.

The experimental setup is introduced in Sec. 2, and the corresponding 1D and 3D computational models are discussed in Sec. 3. In Sec. 4, modeling results with the 1D model demonstrate the impact of restriction at a fixed operating point. Elimination of deep surge is demonstrated by applying compressor inlet restriction to a 3D CFD simulation in Sec. 5. Finally, concluding remarks are included in Sec. 6.

2 EXPERIMENTAL SETUP

The turbocharger of this study is from the right-bank of a twin, parallel turbocharged V6 TiVCT GTDI production engine. The compressor design consists of a vaneless diffuser, no casing treatment (such as a ported shroud), a 6 + 6 (main + splitter) blade impeller with inducer and exducer tip diameters of 35.4 and 46 mm, respectively.

The compressor and system ducting is identical to that of an earlier experimental study[4], where the downstream plenum volume is set to 1.16 L (1/8 of the full volume).

The compressor inlet ducting of the present study incorporates a pneumatic control valve, as shown in Fig. 2. This valve is a Neles RE-Series V-port segment (ball valve with a V-shaped cutout), which fully opens and closes with 90° of rotation. As the valve begins to open (from the closed position), the small end of the V-profile opens first, allowing for more gradual change in cross-sectional flow area with rotation angle at small openings. The valve has an axial length of 103 mm, and the port face (restriction) is located 36 mm from the upstream side. To relate the compressor inlet geometry to dimensions identified in Fig. 1, the valve length is simplified by splitting it into two components up and downstream of the port, which are added to the adjacent duct lengths. The duct upstream of the valve breathes air from ambient through a bellmouth opening and has an effective length of $L_0 = 106$ mm. Between the valve and the compressor inlet, a "short" duct was studied experimentally[4], with an effective length of $L_1 = 391$ mm (axial distance from the valve port to the leading edge of main impeller blades).

Locations that are utilized to present results in the compressor inlet and outlet ducts (1 and 2, respectively, in Fig. 1) are identical for experimental and computational results. Therefore, upstream of the compressor, location 1, is 31.8 mm from connection between the compressor inlet duct and compressor, and downstream of the compressor, location 2, is 49.3 mm from the connection between the outlet duct and compressor[13,14].

Example sound pressure level (SPL) versus frequency spectra from the compressor inlet duct transducer are shown in Fig. 3 for operation at time-averaged conditions of $N_{cor} = 80$ krpm and $\dot{m}_{c,cor} = 10.6$ g/s. The unrestricted compression system operates in deep surge with cross-sectional averaged flow reversal over a portion of the cycle. Large amplitude fluctuations with a fundamental frequency of 21.3 Hz and multiple harmonics (at integer multiples of the fundamental frequency) are also distinguishable in Fig. 3, for the unrestricted system operating in deep surge. When the compressor inlet restriction is utilized to stabilize the system at the same time-averaged operating condition as the unrestricted system, the SPL peaks at the fundamental surge frequency and its harmonics disappear, as shown in Fig. 3. Therefore, all indications of surge are eliminated when sufficient compressor inlet restriction is utilized.

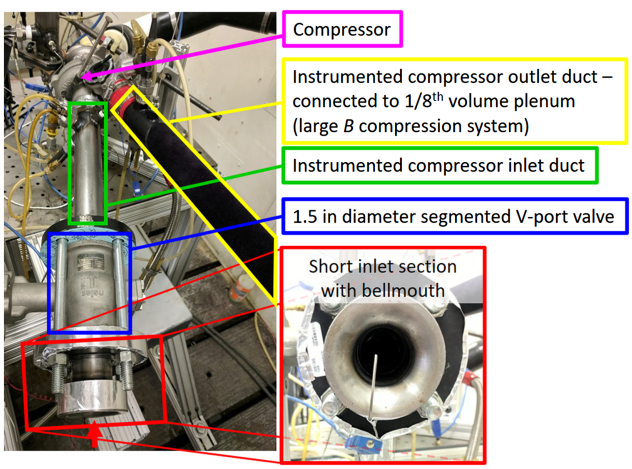

Fig. 2—Experimental setup with control valve installed in the inlet duct.

3 COMPUTATIONAL MODELS

Two computational models are utilized to study different aspects of compressor inlet restriction. A 1D model is used to perform a parametric study of the restriction area ratio at a fixed compressor operating point, in order to provide insight into characteristics of the flow field that lead to stabilization with sufficient restriction. Nevertheless, 1D codes are inherently unable to capture multi-dimensional flow fields, and implementation of compressor performance maps in 1D codes is based on the assumption of quasi-steady operation along the compressor steady-state characteristic. Therefore, a 3D model is also utilized to capture multi-dimensional aspects of the flow field and unsteady compressor behavior when inlet restriction is instantaneously applied during operation in deep surge. Note that the area ratio ($AR = A_r/A_d$) adopted in the present work is the geometric quantity, which is the physical cross-sectional area of flow for the restriction (A_r) relative

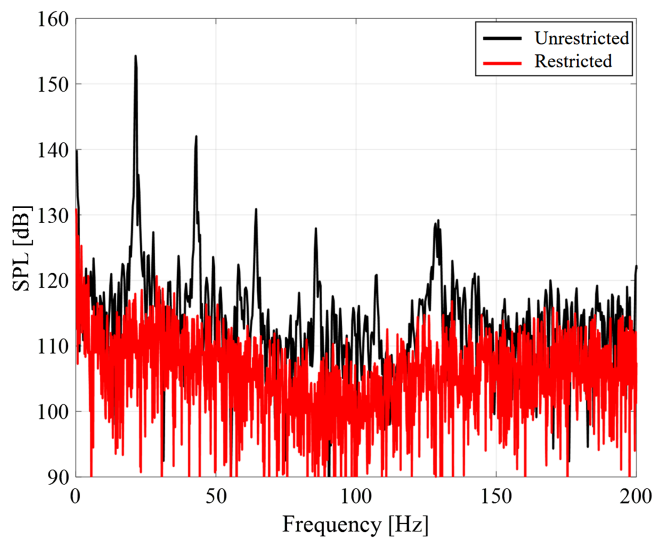

Fig. 3—Comparison of experimental spectra from the compressor inlet duct transducer for the unrestricted and restricted inlet configurations at time-averaged N_{cor} = 80 krpm and 10.6 g/s.

to the adjacent downstream duct (A_d), while the previous analytical approach[4] utilized the cross-sectional area of the vena contracta for A_r.

3.1 One-dimensional Gas Dynamics Model

A 1D gas dynamics model of the turbocharger compression system was constructed both with and without inlet restriction, utilizing the GT-Power[15] software. The ducting portion of the model for the unrestricted system is identical to the "1/8th plenum volume Large *B* system" of Ref. 10, with the exception of increasing the length for the compressor inlet duct by 103 mm, to represent the additional axial length of the fully opened valve. The restricted compressor inlet model splits the compressor inlet duct into two individual duct components, as shown in Fig. 4, representing the portions up and downstream of the restriction. A concentric orifice is located between the compressor inlet duct components, and its diameter is adjusted to achieve the desired restriction. The ducting of the compression system is modeled using straight pipes with constant, circular cross-sections and a "flow-split" at the end of the plenum where both the inlet and exit are connected, as shown in Fig. 4. The bellmouth of the compressor inlet duct is connected to an ambient boundary condition, with temperature and pressure defined as 298 K and 98.05 kPa (equal to conditions in the lab during the corresponding experiment), respectively. A circular orifice is used to represent the control valve downstream of the plenum ("compressor outlet control valve"), and the diameter is held constant at 12 mm (based on modeling results for the unrestricted case). The outlet boundary condition is specified as a constant mass flow rate of 10.6 g/s.

The turbocharger portion of the present 1D model is similar to the previous study[10], with the exception of the experimental data utilized to generate the performance map and elimination of corrections for rotational speed and mass flow rate during reverse flow. The compressor is modeled using a 0D actuator disk and two ducts representing the equivalent geometry of the compressor inlet and exit. The compressor performance information in Fig. 5 is generated (utilizing a Matlab pre-processing script) from the compressor alone characteristics of the extended flow range restricted compressor inlet experimental data (as opposed to the small *B* experimental data in Ref. 10). This compressor performance map is input in the form of a text file to the actuator disk model component and used as a lookup table.

Compressor corrections (for stagnation temperature and pressure at the typical compressor inlet location) that are typically employed to reduce the dependence on inlet conditions are eliminated from the 1D model when flow is reversed. Therefore, the actual rotational speed and mass flow rate are utilized during the reverse flow portion of deep surge cycles, eliminating the step-change in values when the temperature at the (typical) compressor inlet changes instantaneously with flow direction. The "Reverse Flow Implementation" portion of the model was developed to facilitate nonzero compressor power during reverse flow, where the reverse flow portion of Fig. 5 is used as lookup table. The turbine is replaced by a drive torque applied to the turbocharger shaft for simplification.

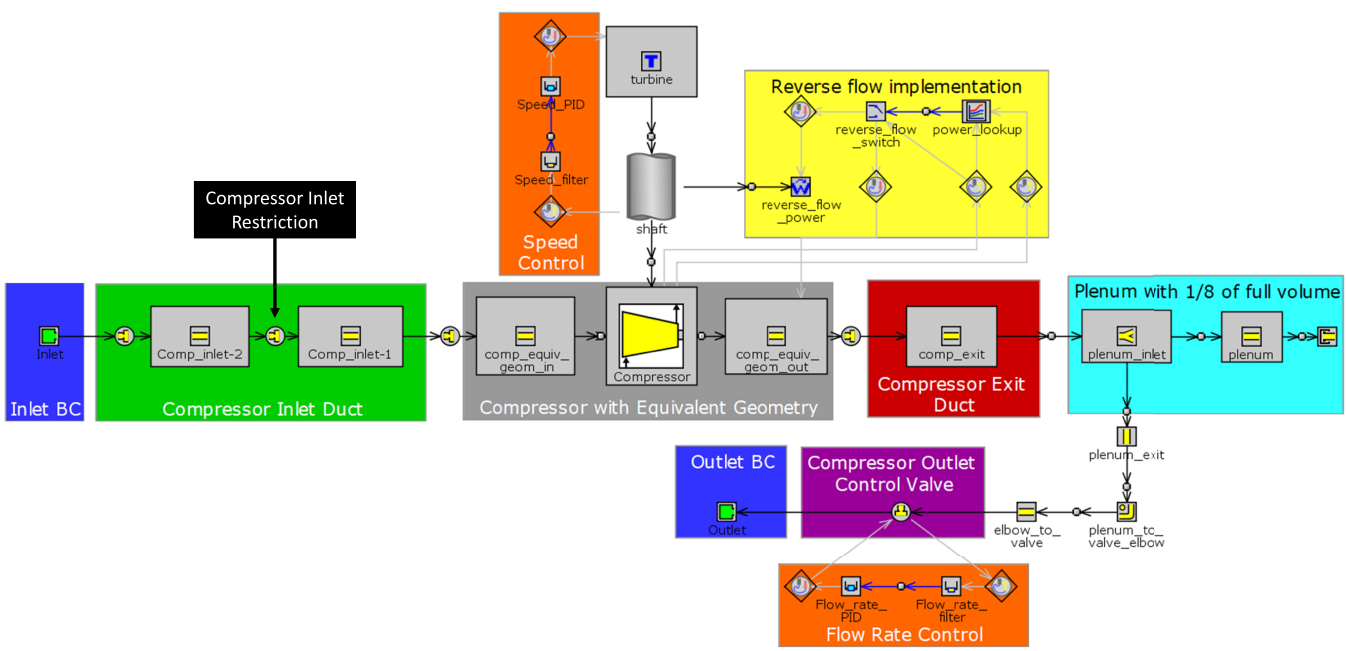

Fig. 4—One-dimensional turbocharger stand compression system model with inlet restriction.

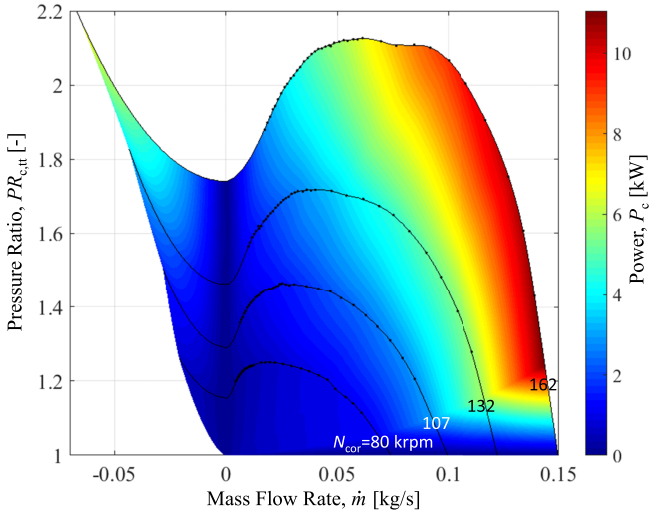

Fig. 5—Compressor performance map for 1D predictions with extrapolations and interpolation.

3.2 Three-dimensional Computational Fluid Dynamics Model

A 3D CFD model of the turbocharger compression system was constructed both with and without inlet restriction, utilizing the STAR-CCM+[16] software. Due to orders of magnitude difference in the surge and impeller rotational frequencies, extensive computing resources are required to carry out these simulations, which was made possible by the Ohio Supercomputer Center[17]. Modeling results with the unrestricted system operating in mild and deep surge are covered extensively in Refs. 10, 11 and 12, respectively. The present study will focus on applying compressor inlet restriction to eliminate the deep surge instability that was observed[12] both experimentally and computationally.

The full compression system model is shown in Fig. 6, while details of the compressor inlet restriction geometry and position are provided in Fig. 7. The "stationary" inlet region (blue in Figs. 6 and 7) consists of the entire compressor inlet duct and the initial portion of the circular cross-section impeller inlet region within the compressor housing. The adjacent "rotating" region (green in Figs. 6 and 7) begins an axial distance of 26.4 mm upstream of the leading edge of the main impeller blades and extends a radial distance of 3 mm into the diffuser. The neighboring stationary compressor outlet region (red in Figs. 6 and 7) consists of the remainder of the diffuser, the volute, compressor outlet duct, plenum, and plenum outlet duct.

The computational model utilizes rigid body motion to rotate the volume mesh surrounding the impeller (rotating region) relative to the stationary inlet and outlet regions. Therefore, the rotational speed of the compressor

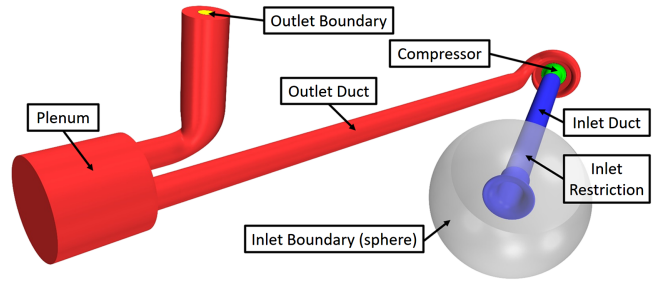

Fig. 6—Model of compression system utilized for 3D CFD predictions.

is constant at the prescribed value of 80 krpm. A pair of internal interfaces is implemented between the rotating and stationary domains, such that mass, momentum, and energy can pass between regions.

The inlet boundary is a sphere centered about the bellmouth opening of the compressor inlet duct, as shown in Fig. 6, which allows for sufficient distance between the constant stagnation (total) pressure boundary and the asymmetric flow field resulting from the presence of the restriction. The inlet boundary condition is set equal to the laboratory barometric pressure of 98.05 kPa and ambient temperature of 298 K at the time of experiments. The inlet boundary is a free stream type that is non-reflective for disturbances that are normal to the surface. At the outlet boundary, the cross-sectional flow area of the compressor outlet control valve is simplified as an 18-mm diameter surface, as shown in Fig. 6. The mass flow rate is adjusted at the outlet boundary to change the compressor operating point along a line of constant rotational speed. The compressor outlet boundary represents the downstream extent of the compression system as the pressure drops across this valve to near the barometric value.

The compressor inlet restriction is representative of the actual control valve geometry at a small opening, where the flow area is confined to a region near the duct wall, as shown in Fig. 7. The cross-sectional flow areas of the compressor inlet duct and restriction are 1192 and 131.3 mm^2, respectively, such that the geometric area ratio of the computational model is $AR = 0.11$. Due to the difference in valve geometries between the 1D and 3D models, a direct comparison in terms of AR should be avoided. Rather, the pressure drop across the inlet restriction will be utilized to compare the two modeling approaches.

The mesh of the 3D CFD model is comprised of unstructured polyhedral cells with prism layers at solid surfaces to better capture near-wall gradients. The total cell count for the full compression system model with inlet restriction (recall Fig. 6) is comprised of approximately 2.2 M cells, which is an increase of approximately 480 k cells relative to the unrestricted compressor inlet model[10–12]. The working fluid is standard air with constant

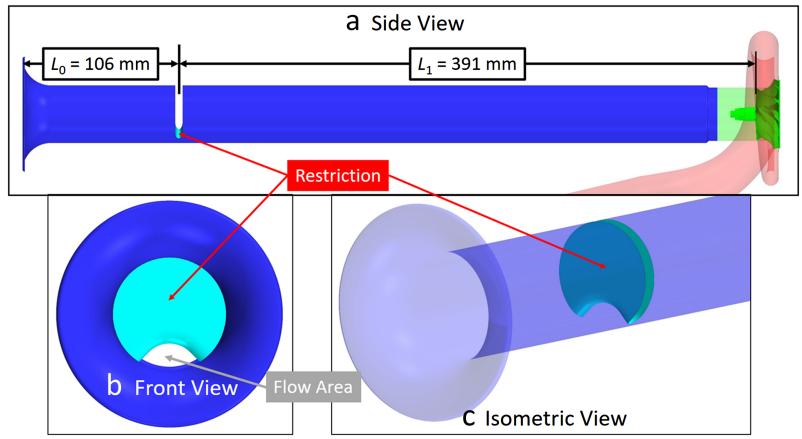

Fig. 7—Compressor inlet restriction of 3D CFD model, including (a) Side view, (b) Front view (from inlet bellmouth), and (c) Isometric view with transparent inlet duct.

properties, and the compressible ideal gas model is utilized for calculation of density. At boundaries with solid surfaces, the adiabatic thermal and no-slip shear stress conditions are employed. The unsteady, Reynolds-Averaged Navier-Stokes (URANS) model is utilized for simulations in the present work, and closure is provided by the *k-ω* (turbulent kinetic energy-specific dissipation rate) turbulence model with the SST (shear stress transport) boundary layer transition model. The coupled flow model with implicit integration method is elected with second-order spatial and temporal discretization.

4 IMPACT OF RESTRICTION ON STABILITY (1D)

The 1D compression system model is utilized in this section to illustrate the impact of compressor inlet restriction on stability. All simulations are carried out at a rotational speed of 80 krpm and an actual mass flow rate of 10.6 g/s. At 80 krpm, the *experimental* deep surge boundary for the *unrestricted* system ($AR = 1$) occurs at a mass flow rate of 11.6 g/s. Therefore, the selected mass flow rate for simulations is approximately 8.6% lower than the deep surge boundary of the unrestricted system. A total of thirty-eight discrete area ratios were studied computationally, in the range of 1 (no restriction) to 0.13, as shown in Fig. 8. In Fig. 8, the time-averaged mass flow rate (taken at the 0D actuator disk) of 10.6 g/s, at each of the studied *AR*, is shown as a solid circle, and the fluctuation ranges (minimum and maximum values) for each *AR* are indicated by vertical bars. Based on the compressor mass flow rate fluctuations, two distinct modes are identified, including stable and deep surge. Over a majority of the *AR* range ($0.29 \leq AR \leq 1$), the compression system operates in deep surge, with the minimum flow rate (bottom of the vertical fluctuation range bars) crossing zero. However, the amplitude of mass flow rate fluctuations reduces with further restriction in this deep surge operating region. A further reduction of restriction area ratio to $AR \leq 0.28$ provides sufficient restriction to eliminate surge instabilities, and the compression system is stabilized. Note that the amplitude of mass flow rate fluctuations is zero (steady) within the stable region. When $AR < 0.13$, the maximum obtainable mass flow rate falls below the target value of 10.6 g/s (pressure drop of the restriction exceeds the pressure rise of the compressor). Of the thirty-eight discrete area ratios, five are selected for detailed, time-resolved comparisons. These five selected restrictions are identified by color in Fig. 8, including $AR = 1$ (dark blue), 0.46 (light blue), 0.29 (green),

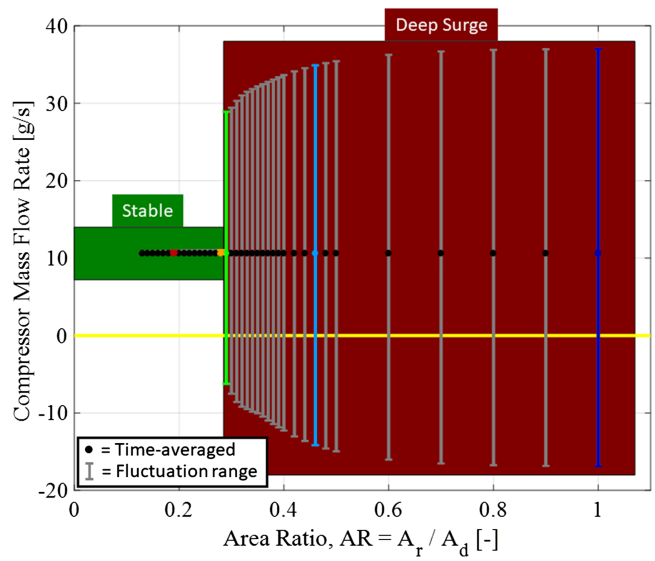

Fig. 8—Compressor mass flow rate (time-average and fluctuation range) as a function of inlet restriction area ratio for 10.6 g/s at 80 krpm.

0.28 (orange), and 0.19 (dark red), where this color coding is implemented consistently throughout the present section.

The time-averaged absolute static pressures at the compressor inlet (p_1) and outlet (p_2) duct locations (identical to experimental setup), along with the corresponding fluctuation ranges, are shown in Figs. 9a and 9b, respectively. Both up and downstream of the compressor, the time-averaged pressures exhibit local minimum and maximum near the mid ($0.28 \leq AR \leq 0.29$) restriction range. The optimal restriction for this operating condition occurs at $AR = 0.28$, which is the minimum restriction (maximum AR) capable of stabilizing the system and results in the maximum time-averaged compressor outlet pressure. For area ratios below ($AR < 0.28$) the optimal restriction, the pressures at the compressor inlet and outlet duct locations decrease rapidly with further restriction, which is counterproductive.

The fluctuation ranges of the compressor inlet and outlet pressures are also shown in Fig. 9. In general, compressor inlet duct pressure fluctuations increase in amplitude as the restriction is closed within the deep surge region ($1 \leq AR \leq 0.29$), and the amplitude in the outlet duct likewise decreases. Further reduction of the area ratio to $AR \leq 0.28$ eliminates pressure fluctuations, as the system is stabilized with sufficient inlet restriction.

Also shown in Fig. 9a (dotted black line) is the predicted pressure downstream of the restriction, under steady conditions (from a simplified model excluding the compressor). For high and low values of AR, time-averaged p_1 is nearly identical to the steady flow value. However, for intermediate ($0.29 \leq AR \leq 0.5$) restrictions, the time-averaged compressor inlet pressure is below that of the restriction alone case under steady flow conditions. The additional time-averaged pressure drop in this intermediate AR range is a result of the increased maximum forward flow (positive) velocity at the restriction throat, as shown in Fig. 10a. The instantaneously high forward throat velocity results in a large pressure drop across the restriction, relative to the steady flow case in Fig. 10b.

Of the thirty-eight discrete area ratios in Figs. 8 through 10, a subset of five (with time-averaged operating points colored other than black) restriction AR were selected to clearly demonstrate the observed trends, including 1, 0.46, 0.29, 0.28, and 0.19. The time-resolved compressor mass flow rates for this subset of studied AR are shown in Fig. 11. The initial ($t < 0$) portion of all time-resolved results in Figs. 11 to 14 is deep surge with the unrestricted ($AR = 1$) system at a time-averaged mass flow rate of 10.6 g/s and rotational speed of 80 krpm. At $t = 0$ (identified by the vertical black line in Figs. 11 to 14), the diameter of the restriction is instantaneously adjusted to change from $AR = 1$ to the corresponding value identified in the legend. A transition period occurs immediately after the diameter of the restriction is reduced, after which, the system either remains in deep surge or transitions to stable operation. The decreasing amplitude of compressor mass flow rate fluctuations with reducing AR is observable on the right-hand side of Fig. 11. In addition, the period of deep surge cycles increases (frequency decreases) as AR is reduced, as shown for AR = 1, 0.46, and 0.29 in Fig. 11. Further restriction of the compressor

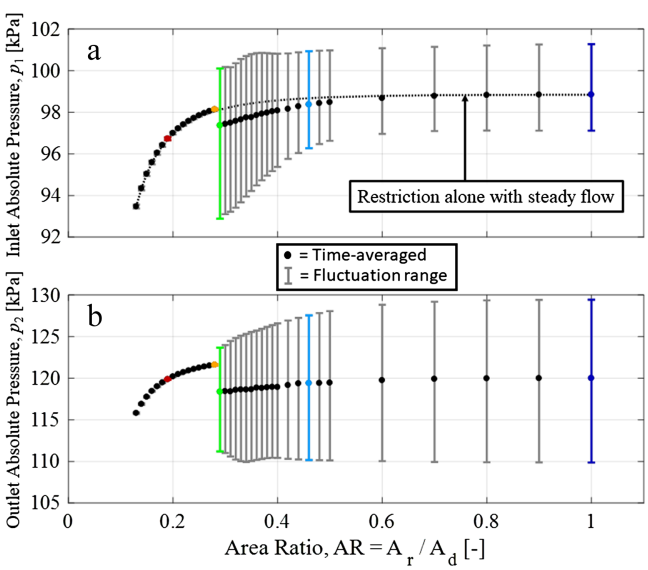

Fig. 9—Predicted absolute static pressure at the compressor (a) Inlet and (b) Outlet duct locations as a function of area ratio at 10.6 g/s and 80 krpm.

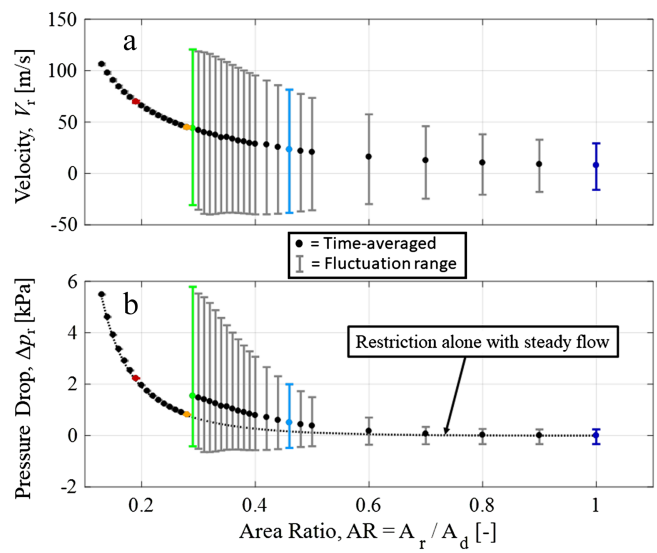

Fig. 10—Predicted restriction (a) Throat velocity and (b) Pressure drop as a function of area ratio at 10.6 g/s and 80 krpm.

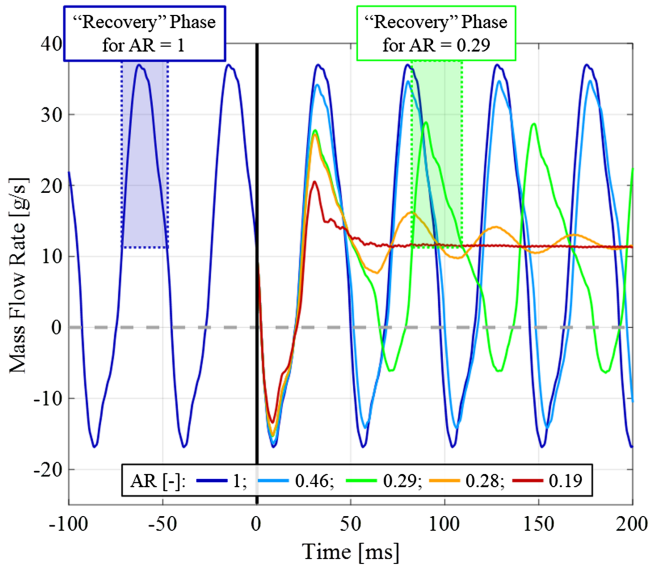

Fig. 11—Time-resolved compressor mass flow rate at discrete inlet restriction area ratios for 10.6 g/s at 80 krpm.

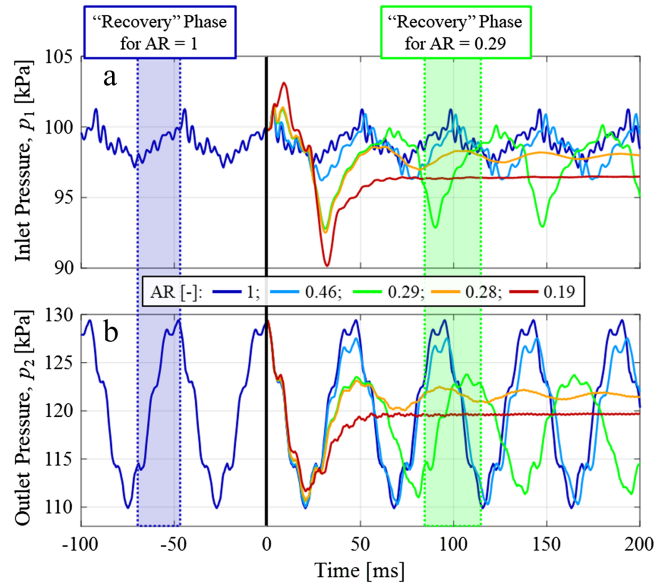

Fig. 12—Time-resolved absolute pressure at discrete inlet restriction area ratios for 10.6 g/s at 80 krpm for the (a) Inlet and (b) Outlet duct locations.

inlet, to AR = 0.28, results in a decaying, low-amplitude mild surge fluctuation, which ultimately disappears beyond $t > 200$ ms of Fig. 11. Therefore, surge instabilities are eliminated for $AR \leq 0.28$. Further restricting the compressor inlet to AR = 0.19 results in a more rapid elimination of surge, and stable operation is achieved within the duration of approximately two deep surge cycles.

The corresponding time-resolved pressures for the subset of five AR are shown for the compressor inlet (p_1) and outlet (p_2) duct locations in Figs. 12a and 12b, respectively. Just after the restriction is applied (for $2.4 < t < 21.2$ ms), the compressor flow rate reverses (for all cases), and the presence of the restriction causes the compressor inlet pressure to increase, as shown in Fig. 12a. As the flow direction switches back to the forward direction (at $t = 21.2$ ms), the restriction causes the compressor inlet pressure to decrease. As expected, the largest increase and decrease in p_1 during this transition period occur with the smallest studied area ratio of 0.19.

Since both 1D and 3D computational results are provided for the unrestricted and most restricted ($\Delta p_r = 2.2$ kPa) configurations, detailed discussion regarding the system behavior immediately following application of the inlet restriction is deferred to the following section. The remainder of this section will focus on the impact of intermediate restriction, which still results in deep surge, on the unstable system behavior. Therefore, the time-resolved 1D computational results for the least ($AR = 1$) and most (AR = 0.29) restricted *deep* surge cases will be utilized next.

The dominant aspect of the deep surge cycle that is altered by the presence of inlet restriction is the amplitude of mass flow rate fluctuations, where the maximum and minimum values occur during the "recovery" and flow reversal phases. The instantaneous fluid properties in the intermediate volume between the restriction and compressor dictate this behavior, as will be described next for the recovery portion of the cycle. The recovery phase is defined as $\dot{m} > \overline{\dot{m}}$, where $\overline{\dot{m}} = 10.6$ g/s is the time-averaged mass flow rate. In Figs. 11 through 14, the recovery portion of a single (of the numerous available) deep surge cycle is identified for $AR = 1$ and 0.29. During this recovery phase, the instantaneous compressor flow rate is in the forward direction and the compressor outlet pressure (p_2) increases. In order to relate the instantaneous flow fields for the restriction and compressor inlet, the time-resolved throat velocity and pressure drop across the restriction are shown in Figs. 13a and 13b, respectively. Over a majority of the recovery phase, the restriction throat velocity is elevated. For the most restricted deep surge case (AR = 0.29) included in Fig. 13a, relative to the unrestricted system ($AR = 1$), the maximum velocity at the throat of the restriction is nearly three times greater, due to the reduced cross-sectional area. Despite this large increase in amplitude of restriction throat velocity with restriction during deep surge, the amplitude of velocity fluctuations in the compressor inlet and outlet ducts decreases (relative to that of the unrestricted case), due to the increased resistance in the system, as shown in Fig. 14.

The pressure drop for the unrestricted case, in Fig. 13b, is slightly non-zero due to unsteadiness of the flow, resulting in the acceleration and deceleration at this location. As the restriction area ratio is reduced to 0.29,

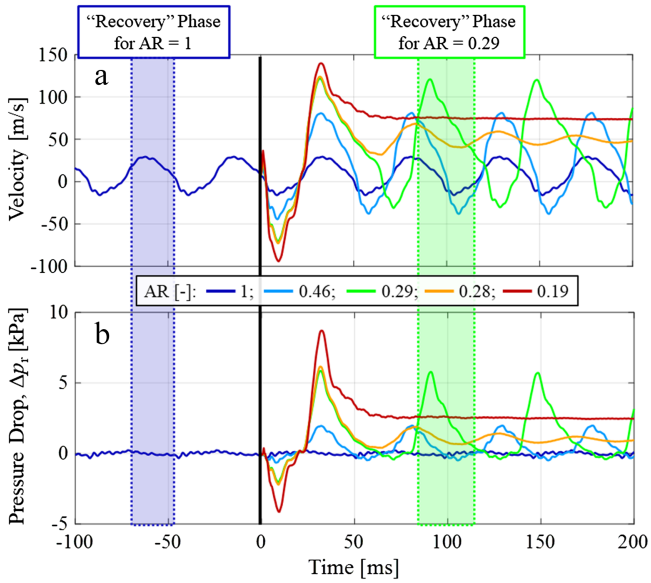

Fig. 13—Time-resolved restriction (a) Throat velocity and (b) Pressure drop as a function of area ratio at 10.6 g/s and 80 krpm.

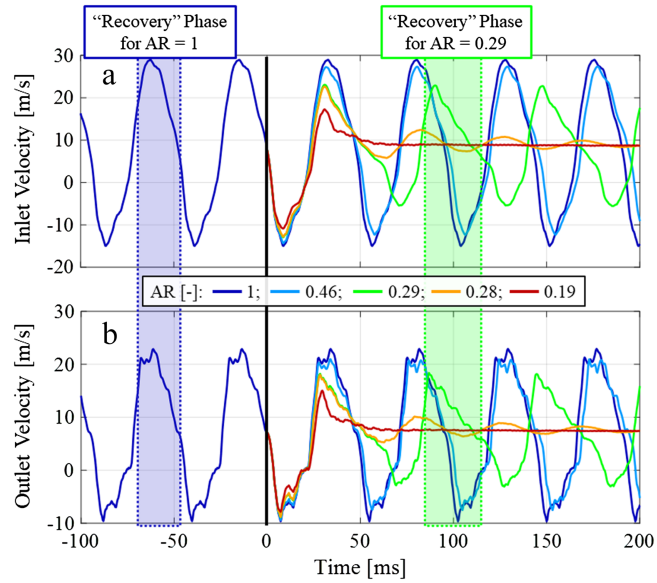

Fig. 14—Time-resolved velocity in the compressor (a) Inlet and (b) Outlet ducts as a function of area ratio at 10.6 g/s and 80 krpm.

the reduced cross-sectional area of the restriction and increased throat velocity (recall Fig. 13a) lead to an elevated instantaneous pressure drop during the recovery phase, as shown in Fig. 13b (also apparent in Fig. 12a). As a result, the density of air at the compressor inlet is lower for the restricted inlet case relative to the unrestricted during the recovery phase. Therefore, as the restriction is closed within the deep surge operating range ($0.29 < AR < 1$), the maximum mass flow rate of the deep surge cycle also reduces, due to the lower instantaneous density and velocity of air between the restriction and compressor. As a result, the duration of the cycle is prolonged, due to the additional time required to pressurize the volume of compressed air (increase p_2).

During the flow reversal ($\dot{m} < 0$) portion of the deep surge cycle, the opposite trend occurs with the pressure at the compressor inlet, although to a lesser extent. With the pressure at the compressor inlet somewhat elevated, flow reversal is resisted by the inlet restriction, and the minimum (reversed) mass flow rate increases (absolute value decreases). Therefore, during unsteady operation in deep surge, mass storage in the intermediate volume, between the restriction and compressor, is the mechanism which causes a reduction in the amplitude of compressor mass flow rate fluctuations.

The time-resolved mass flow rate (recall Fig. 11) and pressures (recall Fig. 12) at the compressor boundaries are combined in Fig. 15 to plot the instantaneous compressor operating points on the performance map. For the three highest *AR* (1, 0.46 and 0.29) shown in Fig. 15, it is observable that the compressor inlet restriction modestly reduces the height (pressure ratio) and significantly shrinks the width (mass flow rate) of the deep surge loop. However, the time-averaged pressure ratio remains nearly constant with decreasing *AR* for these deep surge cases shown in Fig. 15. For $AR = 0.28$ and 0.19, surge fluctuations are eliminated, and the system is stabilized. During stable operation, the compressor operates on the steady-state characteristic, with a marked increase in the time-averaged pressure ratio. The stable operating points, at $AR = 0.28$ and 0.19, do not change with time, so the time-averaged and time-resolved operating point are identical.

5 TRANSIENT STABILIZATION OF DEEP SURGE (3D)

The present section demonstrates the effectiveness of compressor inlet restriction at eliminating surge instabilities through 3D CFD modeling. Simulations both with and without compressor inlet restriction will be compared at an identical (time-averaged) compressor operating point that resulted in deep surge (both experimentally and computationally) with the unrestricted system. The selected operating point is identical to that of the 1D simulations of the previous section, and the compressor inlet restriction is also instantaneously applied during operation in deep surge, in order to assess the ability to actively eliminate surge and capture the unsteady response. In order to isolate the impact of compressor inlet restriction, all other geometric and solver parameters are unchanged between the unrestricted and restricted 3D CFD models.

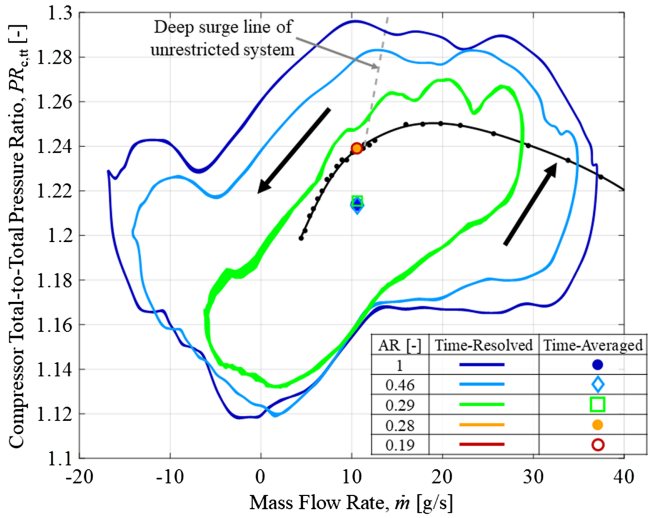

Fig. 15—Predicted compressor operating points with varying compressor inlet restriction at 10.6 g/s and 80 krpm.

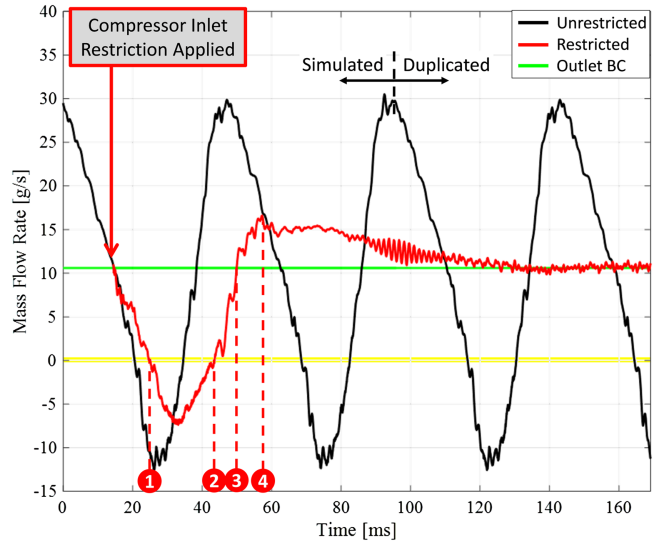

Fig. 16—Comparison of predicted compressor mass flow rate with and without inlet restriction at N_{cor} = 80 krpm and 10.6 g/s.

An extensive analysis was presented in Ref. 12 of the *unrestricted* compression system of the present configuration operating in deep surge at a time-averaged rotational speed and mass flow rate of 80 krpm and 10.6 g/s, respectively. Unrestricted simulations from this previous study[12] are presented in Figs. 16 to 19, as a baseline and reference point for the restricted compressor inlet predictions of the present work. This unrestricted 3D CFD simulation demonstrated close agreement with the measured pressure fluctuations in the compressor inlet and outlet ducts, and the predicted cross-sectional averaged mass flow rate reversed through the compressor during a portion of the surge cycle, as shown in Fig. 16. In addition, the time-resolved compressor inlet (p_1) and outlet (p_2) pressures are presented in Figs. 17 and 18, respectively. Within Figs. 16 to 18, the first two complete deep surge cycles were simulated ($t \leq 95.4$ ms), and the cyclic fluctuations are duplicated over the final 74.5 ms (1.56 cycles), in order to provide a longer duration baseline reference for comparison with the restricted compressor inlet results.

A 3D CFD simulation was carried out for a single inlet restriction, and the 1D computational simulation at $AR = 0.19$ was selected as the case to reproduce, due to the rapid elimination of surge. Due to the difference in restriction geometry for the 1D (concentric orifice) and 3D (recall Fig. 7) models, a one-to-one comparison in terms of AR will be avoided. Rather, the pressure drop across the restriction (for a given flow rate) is utilized to relate the 1D and 3D models. Therefore, the geometric AR of the 3D CFD prediction was set to 0.11, in order to obtain a pressure drop across the restriction equal to 2.2 kPa (recall dark red circle in Fig. 10b).

The CFD model of the compression system with unrestricted inlet was the starting point for the restricted compressor inlet simulation. The compressor inlet valve geometry was incorporated, and the inlet region was remeshed to incorporate this restriction. The flow field from the unrestricted inlet was interpolated onto the new mesh with the restriction, and the simulation was resumed. Therefore, this approach represents an instantaneous change in compressor inlet restriction from fully open ($AR = 1$) to a geometric area ratio of 0.11. The restricted inlet simulation was started at 14.5 ms, as shown in Figs. 16 to 18, when the mass flow rate (10.6 g/s) through the compressor is equal to that imposed at the outlet boundary (recall Fig. 16), and the outlet pressure is near the maximum value throughout the precursor deep surge cycle (Fig. 18). In Figs. 16 to 18, four additional instances of time are also identified for use throughout the following discussion, including 25.0, 43.5, 49.9, and 57.6 ms, which are sequentially numbered as "points" 1 to 4. Due to the unsteady dynamics of the deep surge cycle utilized for initialization, the restricted compressor inlet modeling results are similar to those of the unrestricted system for just a short period immediately following the application of the restriction. The compressor mass flow rate of the restricted inlet case in Fig. 16 then quickly deviates from that of the unrestricted system, as the time rate of mass flow rate change ($d\dot{m}_c/dt$) increases. Additionally, the minimum mass flow rate of the restricted system is higher (absolute value is lower) than the unrestricted configuration. While flow is reversed through the compressor and inlet restriction ($25.0 \leq t \leq 43.5$ ms [between points 1 and 2]), the restriction is now working in

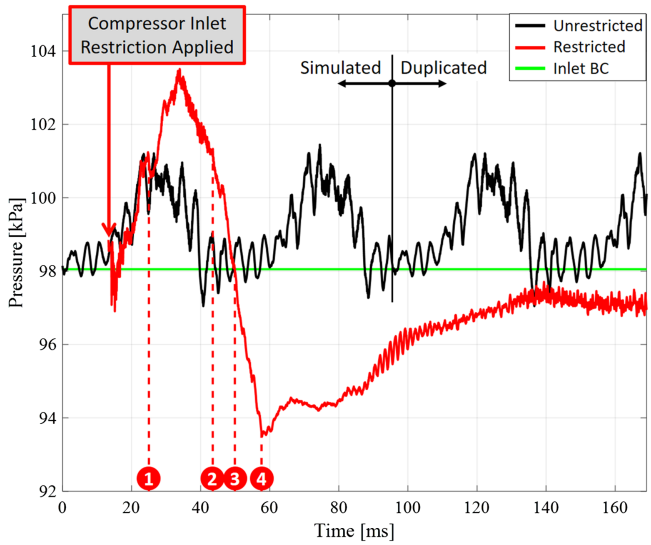

Fig. 17—Comparison of predicted compressor inlet pressure with and without inlet restriction at N_{cor} = 80 krpm and 10.6 g/s.

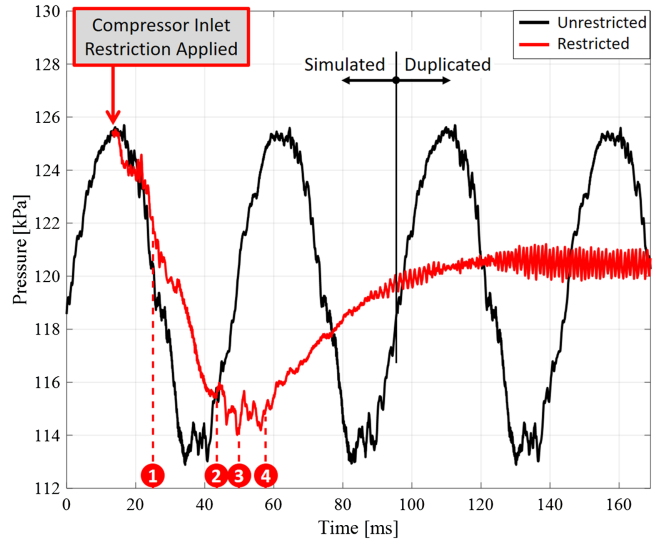

Fig. 18—Comparison of predicted compressor outlet pressure with and without inlet restriction at N_{cor} = 80 krpm and 10.6 g/s.

the reverse direction (pressure decreases in the direction of flow), and mass storage in this intermediate (between the restriction and impeller) volume results in a rapid elevation of compressor inlet pressure, as shown in Fig. 17. Over this same duration ($25.0 \leq t \leq 43.5$ ms [between points 1 and 2]), flow reversal through the compressor also causes the pressure at the compressor outlet to reduce for both simulations. However, the presence of the inlet restriction increases both the time rate of compressor outlet pressure change (dp_2/dt) and the minimum pressure.

As the flow rate recovers back to the forward direction (at $t = 43.5$ ms [point 2] in Fig. 16) for the restricted compressor inlet prediction, the pressure begins to decrease rapidly in the portion of the inlet duct between the restriction and compressor inlet, as shown in Fig. 17. Now ($43.5 < t < 49.9$ ms [between points 2 and 3]), flow is exiting the intermediate duct volume through both the compressor and the restriction ($p_1 > p_0$). After p_1 reduces below p_0 ($t > 49.9$ ms [point 3]), flow through the compressor inlet restriction returns to the forward direction for the remainder of the simulation.

The flow rate through the compressor continues to increase until it reaches a maximum of 16.5 g/s at $t = 57.6$ ms (point 4). As a result, the flow rate through the restriction increases, and the compressor inlet pressure (p_1) simultaneously reaches its minimum value. From this point ($t = 57.6$ ms [point 4]) on, the compression system recovers relatively smoothly to the final operating condition that is free of (mild or deep) surge instabilities. The experimental counterpart is shown in the frequency domain in Fig. 3. Both the computational (time domain in Fig. 17) and experimental (frequency domain in Fig. 3) results demonstrate elimination of surge instabilities through compressor inlet restriction.

The time-resolved compressor operating points of the unrestricted and restricted CFD simulations are superimposed with the steady-state compressor performance data at the corresponding rotational speed of 80 krpm in Fig. 19. The two simulated deep surge cycles from the unrestricted system are essentially identical (converged), illustrating that the system has reached a repeating amplitude, cyclic structure. As the compressor inlet restriction

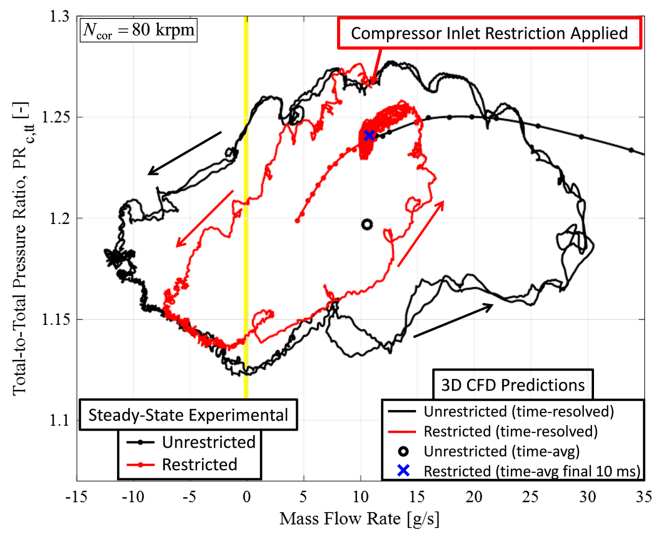

Fig. 19—Comparison of predicted compressor operating points with and without restriction at N_{cor} = 80 krpm and 10.6 g/s.

is applied, the instantaneous compressor operating point is near the top of the surge loop (identified in Fig. 19), and it moves in the counter-clockwise direction. The trajectory of the instantaneous operating point for the restricted inlet compression system quickly deviates from that of the unrestricted system, and the surge loop diminishes. In addition, the time-averaged (over the final 10 ms for the restricted simulation and a deep surge cycle for the unrestricted) are also included in Fig. 19. For the restricted system, the total-to-total pressure ratio of the compressor alone is 1.241 (blue "x" in Fig. 19), and the effective (restriction and compressor; recall Eqn. (1)) pressure ratio is 1.228, both of which are significantly higher than the time-average pressure ratio with the unrestricted system ($PR_{c,tt}$ = 1.197 or open black circle in Fig. 19) operating in deep surge.

When the compressor inlet restriction is utilized to eliminate deep surge, the time-averaged temperature at the compressor outlet is reduced from 345.5 to 339.5 K. Therefore, the power required to drive the compressor is also reduced, due to elimination of lost work when compressed air escapes back to the inlet during a portion of the deep surge cycle.

6 CONCLUSIONS

The present study demonstrated that 1D and 3D computational tools can be utilized to model the stabilizing aspects of compressor inlet restriction. The compressor operating point selected for the present work was at a mass flow rate below the deep surge boundary for the selected rotational speed. Therefore, both 1D and 3D simulations with the unrestricted (fully open) system resulted in deep surge. As the inlet restriction was partially closed with the 1D model, the compression system remained in deep surge until the area ratio (of cross-sectional area for restriction relative to adjacent duct) was reduced below a critical value. With partial closings that still resulted in deep surge (above the critical value), the amplitudes of mass flow rate and compressor outlet pressure fluctuations decreased; however, with additional restriction, the amplitude of compressor inlet fluctuations increased. Also, the surge cycle period increased (frequency decreased) as the cross-sectional area of the restriction was reduced during deep surge. The minimum restriction required to eliminate (both mild and deep) surge instabilities was demonstrated to be the optimal value, as the time-averaged compressor outlet pressure reached its maximum value.

The 3D CFD simulations of the present work were carried out at conditions identical to that of selected 1D cases, including the unrestricted system and a small area ratio which rapidly eliminated surge. For equal pressure drop across the restriction, the 1D and 3D CFD simulations demonstrated stabilization within a duration equal to roughly two deep surge cycles, as the compression system transitioned to stable, steady-state operation. Overall, the predicted compression system pressures and flow rates of the 1D and 3D simulations agreed reasonably well, especially in terms of the qualitative behavior. However, the compressor outlet pressure and flow rate oscillations during deep surge were predicted to have higher amplitudes by the 1D model, relative to the corresponding 3D modeling results. Both the 1D and 3D predictions revealed the role of mass balance in the intermediate volume (between the restriction and compressor) toward reducing the amplitude of mass flow rate fluctuations.

7 ACKNOWLEDGMENT

The authors would like to thank the Ohio Supercomputer Center[17] for their generous award of computing resources to carry out these simulations.

8 REFERENCES

1. H. Emmons, C. Pearson, and H. Grant, "Compressor surge and stall propagation", *Trans. ASME*, **77**, 455–469, (1955).
2. T. Yano and B. Nagata, "A study on surging phenomena in diesel engine air-charging system", *The Japan Society of Mechanical Engineers*, **14**, 364–376, (1971).
3. E.M. Greitzer, "Surge and rotating stall in axial flow compressors, part I: theoretical compression system model", *ASME J. Engineering for Power*, **98**, 190–197, (1976).
4. R. Dehner, A. Selamet, and K. Miazgowicz, "Effective suppression of surge instabilities in turbocharger compression systems through a close-coupled compressor inlet restriction", SAE Technical Paper, 2018-01-1714, (2018).
5. R. Dehner, "Simulation of surge in turbocharger compression systems", M.S. thesis, Department of Mechanical Engineering, The Ohio State University, Columbus, OH, (2011).
6. R. Dehner, A. Selamet, P. Keller, and M. Becker, "Simulation of mild surge in a turbocharger compression system", *SAE Int. J. Engines*, **3**(2), 197–212, (2010).
7. R. Dehner, A. Selamet, P. Keller, and M. Becker, "Prediction of surge in a turbocharger compression system vs. measurements", *SAE Int. J. Engines*, **4**(2), 2181–2192, (2011).
8. R. Dehner, A. Selamet, E. Selamet, P. Keller, J. Shutty, K. Tallio, K. Miazgowicz, and R. Wade, "Simulation of surge in the air induction system of turbocharged internal combustion engines", *Noise Control Engr. J.*, **65**(4), 275–287, (2017).
9. R. Dehner, A. Selamet, P. Keller, and M. Becker, "Simulation of deep surge in a turbocharger compression system", *ASME J. Turbomach.*, **138**(11), 111002, (2016).
10. R. Dehner, "An experimental and computational study of surge in turbocharger compression systems", Ph.D. dissertation, Department of Mechanical and Aerospace Engineering, The Ohio State University, Columbus, OH, (2016).
11. R. Dehner and A. Selamet, "Three-dimensional computational fluid dynamics prediction of turbocharger centrifugal compression system instabilities", *ASME J. Turbomach.*, **141**(8), 081004, (2019).
12. R. Dehner and A. Selamet, "Physics of deep surge in an automotive turbocharger centrifugal compression system", *ASME J. Engineering for Gas Turbines and Power*, **141**(6), 061003, (2019).

13. N. Figurella, R. Dehner, A. Selamet, K. Tallio, K. Miazgowicz, and R. Wade, "Noise at the mid to high flow range of a turbocharger compressor", *Noise Control Engr. J.*, **62**(5), 306–312, (2014).
14. R. Dehner, N. Figurella, A. Selamet, P. Keller, M. Becker, K. Tallio, K. Miazgowicz, and R. Wade, "Instabilities at the low-flow range of a turbocharger compressor", *SAE Int. J. Engines*, **6**(2), 1356–1367, (2013).
15. Gamma Technologies, GT-Power (Version 7.4), Westmont, Il, (2015).
16. Siemens, STAR-CCM+ (Version 12.06), Melville, NY, (2018).
17. Ohio Supercomputer Center, Owens Supercomputer, Columbus, OH, (2016).